Publ. Astron. Soc. Japan (2014) 00(0), 1–5
doi: 10.1093/pasj/xxx000

Photometric Redshifts for the Hyper Suprime-Cam Subaru Strategic Program Data Release 3

HSC Collaboration, Atsushi J. Nishizawa[1,2], Bau-Ching Hsieh[3] and Masayuki Tanaka[4]

[1]Gifu Shotoku Gakuen University, 1-1 TakakuwaNishi, Yanaizucho, Gifu, 501-6194, Japan
[2]Nagoya University, Furocho, Chikusa-ku, Nagoya, 464-8602, Japan
[3]Academia Sinica Institute of Astronomy and Astrophysics, 11F of AS/NTU Astronomy-Mathematics Building, No.1, Sec. 4, Roosevelt Rd, Taipei 10617, Taiwan
[4]National Astronomical Observatory of Japan, 2-21-1 Osawa, Mitaka, Tokyo 181-8588, Japan

*E-mail: atsushi.nishizawa@iar.nagoya-u.ac.jp

Received ; Accepted

Abstract

In this article, we present the 3rd public data release of the photometric redshift catalog of the Hyper Suprime-Cam SSP survey. The full catalog can be available online from out data release site, `https://hsc-release.mtk.nao.ac.jp/`.

1 HSC PDR3 photometric data

The PDR3 photometric reshift catalog is computed based on the photometric sample of the HSC PDR3 (S20A) (Aihara et al. 2022). Numerous updates on the dataset and pipeline have been made from PDR2. The PDR3 data includes all the data taken before January 2020, over 278 nights in total. The major updates since PDR2 can be summarized as follows.

1. Deep/Ultra-Deep layers reaches $\sim 80\%$ completeness in the depth.
2. Wide layer has covered 670 deg^2 in terms of FDFC(Full Depth Full Color).
3. exposure times in izy bands are reduced and seeing condition to take i band has been relaxed.
4. Apply the magnitude zero-point offset according to the stellar locus, as a result of new photometric calibration FGCM.
5. Implemented a correction for different filter transmission between $i/i2$ bands and $r/r2$ bands.
6. Improved the PSF modeling and background subtraction.

2 Calibration Sample

To calibrate the photo-z, we collect publicly available spectroscopic redshift samples as well as the private spectroscopic sample. We also use grism redshifts and high accuracy photometric redshift samples in COSMOS. We denote them as reference redshift samples. They are zCOSMOS DR3 (Lilly et al. 2009), 10k DEIMOS (Hasinger et al. 2018), LEGA-C (van der Wel et al. 2016), UDSz (Bradshaw et al. 2013; McLure et al. 2013), 3D-HST (Skelton et al. 2014; Momcheva et al. 2016), FMOS-COSMOS (Silverman et al. 2015), VVDS Final DR(Le Fèvre et al. 2013), VIPERS PDR2 (Scodeggio et al. 2018), eBOSS DR16 (Ahumada et al. 2020), GAMA DR3 (Baldry et al. 2018), C3R2 DR2 (Masters et al. 2019), WiggleZ DR1 (Drinkwater et al. 2010), DEEP2/3 DR4 (Davis et al. 2003; Cooper et al. 2011; Cooper et al. 2012; Newman et al. 2013), PRIMUS DR1 (Coil et al. 2011; Cool et al. 2013), VANDELS DR2 (Pentericci et al. 2018), 2dFGRS (Colless et al. 2001) and 6dFGRS DR3 (Jones et al. 2009). Those catalogs provide a quality control parameter to evaluate the quality of spec-z. As in the PDR1, we construct the homogenized bit flag and it is summarized below for the catalogs which are newly available in this data release. The following criteria should be satisfied before

we match the catalog to the HSC photometric catalog.

– Public spec-z data: common selection

1. $0.01 < z < 9$ (no stars, quasars, or failures)
2. $\sigma_z < 0.005(1+z)$ (error cut).

In addition, for individual catalog, we define the flag to homogenize the quality of the reference sample.

1. zCOSMOS bright: $3 \leq$ `CC` ≤ 4 or `CC` $= 2.4, 2.5$ or $9.3 \leq$ `CC` ≤ 9.5
2. eBOSS : `zWarning` $= 0$ (no apparent issues)
3. GAMA : $4 \leq$ `NQ`
4. UDSz : `Flag` $= 3, 4, A, B$ or $B*$.
5. DEEP2/3 : `qFlag` $= 4$ ($> 99.5\%$ confidence)
6. VANDELS : `zflg` > 2 ($> 95\%$ confident)
7. C3R2 : $3 \leq$ `Qual`.
8. VVDS : `ZFLAGS` $= 3$ or 4
9. DEIMOS : `Qf` $= 2$
10. FMOS : `zflag` ≥ 1
11. LEGA-C : `f_use` $= 1$
12. PRIMUS : `zquality` ≥ 3
13. VIPERS : $n + 2.6 <$ `zflg` $< n + 4.6$ where $n = 0, 10, 20$ or 210.
14. WiggleZ : `Qop` ≥ 4
15. DEEP2/3 : `redshift_flag` ≥ 3
16. 2dFGRS : `quality` ≥ 3
17. 6dFGRS : sum of comparison flags is 0.

– Private spec-z data:
In addition to the public spec-$z$catalogs, we combine private catalogs of COSMOS spec-z's (Mara Salvato, private communication) exclusively used for our photo-z calibration (the private catalog is not included in the HSC PDR3).
– Multiband photo-z data:
In order to cover the deep photometric data of HSC, we also combine COSMOS2015 multiband photo-z(Laigle et al. 2016).

Those spec-z catalogs are matched to the HSC UltraDeep/Deep photometric catalog and subsequently to the HSC Wide catalog which meet the following criteria,

1. `isprimary` is `True` (no duplicates)
2. `[grizy]_cmodel_flux` > 0
3. `[grizy]_cmodel_fluxsigma` > 0

The matching radius is taken to 1 arcsec.

The following quantities are then selected and/or computed:

1. Identifiers: `ID`, (`ra,dec`), and (`tract,patch`) coordinates, but these are confidential during the calibration.
2. Fluxes: `PSF` fluxes, `cmodel` fluxes, `cmodel_exp` fluxes, `cmodel_dev` fluxes, and PSF-matched aperture fluxes with target 1.3 arcsec PSF and 1.5 arcsec apertures, and undeblended PSF matched aperture flux. We also provide the Galactic attenuation estimates (`a_[grizy]`).
3. Shapes: `sdss_shape` parameters.
4. Redshift: redshift, 1σ error when available, parent survey (SDSS, etc.).
5. Depth: flag for UltraDeep/Deep, and Wide photometry.
6. Emulated errors: emulated wide-depth photometric errors for the objects which do not match to the Wide layer data. For each UltraDeep/Deep objects, we assign the mean of the photometric errors over wide layer objects located in the nearest neighbors in the magnitude and color hyperspace.
7. Weights: We compute the specific weights such that the magnitude and magnitude error distribution of the training sample after applying the weights matches to the one for the entire wide layer photometric target sample (Lima et al. 2008). The weights are thus used to optimize the photo-z to maximize the performance of the target photometric sample, and then used to predict the expected performance of the photo-z for the target sample.
8. cross-validation ID: We divide the training sample into 5 subset to conduct a cross validation.

3 Photo-z codes

In the HSC PDR3, photo-z catalogs based on one template fitting code `Mizuki` and empirical-method-based code `DEmP` and deep neural network based code `DNNz` are available. Here, we summarize the method of each photo-z code.

3.1 DEmP

The Direct Empirical Photometric code (DEmP) is an empirical quadratic polynomial photometric redshift fitting code. Details are described in Hsieh & Yee (2014) and Tanaka et al. (2018). As in the previous releases, the photo-z, stellar mass, and SFR are provided, and they are computed from undeblended convolved fluxes independently. The photo-z, as well as stellar mass and SFR, for each object is calculated using the 40 nearest neighbors in a ten-dimensional parameter space (5 magnitude axes, 4 color axes, and the size derived from shape SDSS). There is no number of filters cut, i.e., the output products are provided for objects with even one-band-only

photometry. The PDF of photo-z for each galaxy is generated using Monte Carlo technique and the bootstraping method. We use Monte Carlo technique to generate 500 data sets based on the photometry and uncertainties of the input galaxies to account for the effects due to photometric uncertainties. We then bootstrap the training set for each input galaxy 500 times for each of the Monte Carlo generated data set, to estimate the sampling effect in the training set.

3.2 Mizuki

We use a template fitting-code mizuki. Details are described in Tanaka (2015) and Tanaka et al. (2018), but a brief outline is given here. The code uses a set of templates generated with the Bruzual & Charlot (2003) stellar population synthesis code assuming a Chabrier (2003) IMF and Calzetti et al. (2000) dust attenuation curve. Emission lines are added to the templates assuming solar metallicity (Inoue 2011). Template error functions are incorporated in order to account for systematic offsets and uncertainties in the templates. We apply a set of Bayesian priors on the physical properties and let the priors depend on redshift to keep the template parameters within realistic ranges to reduce the degeneracy in the multi-color space and also to let templates evolve with redshift in an observationally motivated way.

As in the PDR2, the PDF recalibration is applied following Bordoloi et al. (2010), which delivers a small improvement in the overall performance. We use the undeblended convolved fluxes scaled to the cmodel fluxes so that they are reasonably close to the total fluxes.

3.3 DNNz

In PDR3, deep learning code, `DNNz`. DNNz architecture is consist of multi-layer perceptorons with 5 hidden layers. The input layers can handle every types of observable and we use `cmodel fluxes`, `undeblended convolved flux`, `PSF fluxes` and size derived from `shape SDSS`. In total, we have (3 fluxes + 1 size) $\times$ 5 bands = 20 attributes. All fluxes are converted to `asinh` magnitude so that it coinside with AB magnitude at the bright end. magnitude correction due to $i/i2$ and $r/r2$ filter transmission difference has been applied and magnitude offset derived from the stellar locus have been also applied. We observe that adding size information slightly improve the overall photo-z accuracy. For training, 3/5 of the training set is used and 1/5 is used for validation. Rest of the 1/5 is used for the accuracy test presented in this note. We have 100 nodes in the output layer where each of them represents the probability of the galaxy lying at the redshift bin spaning from $z = 0$ to 7. It can approximate the PDF distribution of the galaxy's redshift. We provide the full PDF and point statistics as usual and outlier probability predicted from the `DNNz` architecture. The outlier probability can be used to efficiently remove the outlier. Since `zRisk` or `zConf` is calculated based on the integration of PDF but `DNNz` utilizes full shape of the PDF to descriminate the outliers (Nishizawa et al. in prep.).

4 Performance Evaluation

All the statistics shown in this note is based on the photoz_best, which outperforms traditional point estimates such as mean, median or mode (Tanaka et al. 2018). Exceptionally, only for `DEmP`, `photoz_mode` is usually more accurate than `photoz_best` and therefore the `DEmP` photo-z users may consider using `photoz_mode`, instead of `photoz_best`.

4.1 Scatter plots

Here we show the performance tests with the same metric done in the PDR2 (Nishizawa et al. 2020) Figure 1 shows the object to object comparison between photo-z and reference-z. Upper panels show the raw distribution for the wide sample. Dashed lines are 15% limit. The second row shows the distribution with reweighted to the entire wide photometric sample. The weight has been computed so that the matnitude distributions match to the target sample,

$$P^{\text{all-wide}}(g,r,i,z,y) = \sum_i w_i P^{\text{calib}}(\text{g,r,i,z,y}). \quad (1)$$

In practice, the weight can be calculated by the local object density in the multi-dimensional space of the magnitude for the target sample divided by the local density of the calibration sample about the given object, within a given fixed radius (Lima et al. 2008). The third row shows the close up of the distribution for bright sample (i-mag$<$ 22.5). We see that some fraction of objects in `Mizuki` is lying at $z_p = 0$ and $z_s > 1.0$, which may be caused by the confusion of stars and galaxies. For the latter analysis, we remove the objects $z_p = 0$ as they are readily removed by users. We do not see such population both in `DEmP` and `DNNz`. The bottom row in Figure 1 shows the distribution of dud sample. We can see clear reduction of the scatter and outliers, outside the dashed lines.

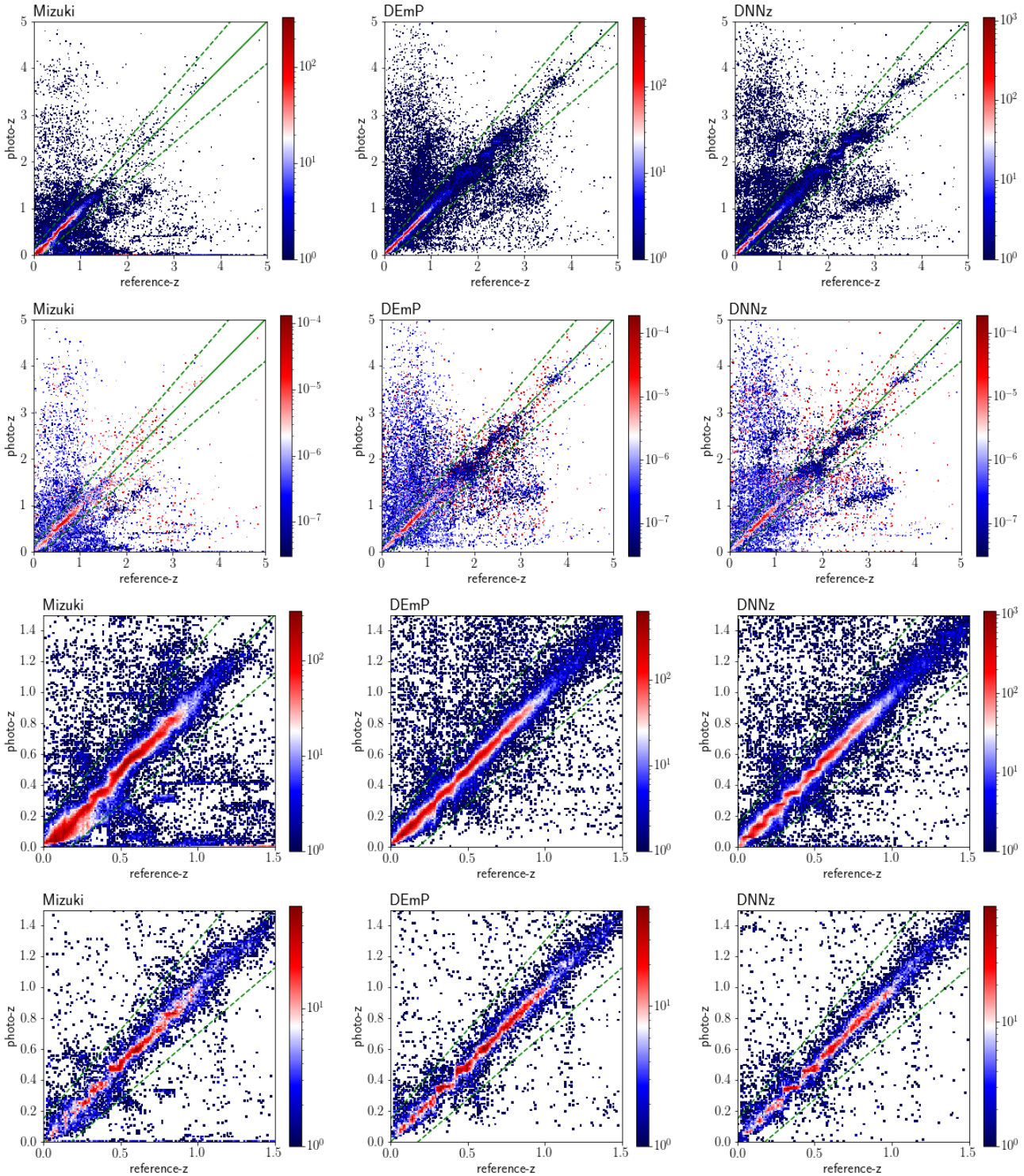

Fig. 1. One-to-one basis comparison between photo-z and reference-z. From left to right, Mizuki, DEmP and DNNz. Upper panels are raw distribution for wide photo-z, second row is reweighted to the entire wide photometric sample, third row is raw distribution but limited to sample brighter than imag 22.5 and the bottom row is raw dud distribution.

4.2 statistics on the point estimates

Figures 2 shows the mean bias, scatter and outlier rate as a function of i-band cut, i.e. the sample brighter than the values in the horizontal axis is selected. As described in the previous section, we remove the objects $z_p = 0$ for `Mizuki`. Upper panels are for wide sample and lower sample for dud sample. ML based methods, `DEmP` and `DNNz` show consistent accuracy for all statistics except that the sign of the bias is positive for `DNNz` but negative for `DEmP`. `Mizuki` shows slightly larger bias and scatter but the outlier rate is almost consistent with others.

4.3 N(z) distribution

In various scientific cases, instead of the individual galaxy's photo-z, the redshift distribution for selected subsample is of great importance. Here in figure 4, we show the redshift distribution for the tomographic binned subsamples, where the bins are defined by the HSC-Y1 cosmic shear analysis (Hikage et al. 2019). The redshift binning is $z = [0.0, 0.3, 0.6, 0.9, 1.2]$. The sample is defined using `photoz_best` for each code. `Mizuki` and `DEmP` spans redshift from 0 to 7 into 700 bins so that they capture the detailed shape of the PDF, while the `DNNz` only have 100 bins but overall shape is consistent with others. We confirm that for `DNNz`, 100 bins are sufficient for predicting point estimate and finner binning does not improve the accuracy statistics. Figure 4 shows the stacked PDF distribution of the tomographic subsamples. The distributions are normalized so that the maximum becomes unity. Shaded and dashed lines are raw distribution for test sample and reweighted distribution, respectively.

4.4 Tests on PDF

The quality of the PDF can be quantified using probability integral transform (PIT). The PIT analysis evaluates that the error of the photo-z is correctly reflected in the PDF. When the PDF is properly calibrated, the histogram will become flat distribution. However, if the PDF is narrow and the photo-z error is underestimated, the PIT distribution will have peaks near 0 and 1 while the PDF overestimates the error, PIT will have peak near 0.5. Figure 5 shows the PIT distributions for wide (upper panel) and dud (lower). For the wide sample, `DEmP` and `DNNz` shows fairly similar shape while the `Mizuki` seem to have slope toward higher value. The interpretation of this behavior is not trivial but at least we can observe that there are two peaks at PIT=0 and 1, which indicates the underestimation of the photo-z error. `DEmP` and `DNNz` also shows similar features but the effect is marginal. For the DUD sample, the PIT distribution is fairly flat which suggests that the PDF is well calibrated except for the spikes at 0 and 1.

All of the catalog products such as photo-z point estimates are available in the database. The full PDFs are stored in the fits format and are available from the photo-z page of the PDR3 site; `https://hsc-release.mtk.nao.ac.jp/`. Tables 1 and 2 shows the available photo-z quantities and number of objects in the database.

References

Ahumada R. et al., 2020, ApJS, 249, 3
Aihara H. et al., 2022, PASJ, 74, 247
Baldry I. K. et al., 2018, MNRAS, 474, 3875
Bordoloi R., Lilly S. J., Amara A., 2010, MNRAS, 406, 881
Bradshaw E. J. et al., 2013, MNRAS, 433, 194
Bruzual G., Charlot S., 2003, MNRAS, 344, 1000
Calzetti D., Armus L., Bohlin R. C., Kinney A. L., Koornneef J., Storchi-Bergmann T., 2000, ApJ, 533, 682
Chabrier G., 2003, PASP, 115, 763
Coil A. L., Weiner B. J., Holz D. E., Cooper M. C., Yan R., Aird J., 2011, ApJ, 743, 46
Colless M. et al., 2001, MNRAS, 328, 1039
Cool R. J. et al., 2013, ApJ, 767, 118
Cooper M. C. et al., 2011, ApJS, 193, 14
Cooper M. C. et al., 2012, MNRAS, 419, 3018
Davis M. et al., 2003, Society of Photo-Optical Instrumentation Engineers (SPIE) Conference Series, Vol. 4834, Science Objectives and Early Results of the DEEP2 Redshift Survey, Guhathakurta P., ed., pp. 161–172
Drinkwater M. J. et al., 2010, MNRAS, 401, 1429
Hasinger G. et al., 2018, ApJ, 858, 77
Hikage C. et al., 2019, PASJ, 71, 43
Hsieh B. C., Yee H. K. C., 2014, ApJ, 792, 102
Inoue A. K., 2011, MNRAS, 415, 2920
Jones D. H. et al., 2009, MNRAS, 399, 683
Laigle C. et al., 2016, ApJS, 224, 24
Le Fèvre O. et al., 2013, A&A, 559, A14
Lilly S. J. et al., 2009, ApJS, 184, 218
Lima M., Cunha C. E., Oyaizu H., Frieman J., Lin H., Sheldon E. S., 2008, MNRAS, 390, 118
Masters D. C. et al., 2019, ApJ, 877, 81
McLure R. J. et al., 2013, MNRAS, 428, 1088
Momcheva I. G. et al., 2016, ApJS, 225, 27
Newman J. A. et al., 2013, ApJS, 208, 5
Nishizawa A. J., Hsieh B.-C., Tanaka M., Takata T., 2020, arXiv e-prints, arXiv:2003.01511
Pentericci L. et al., 2018, A&A, 616, A174
Scodeggio M. et al., 2018, A&A, 609, A84
Silverman J. D. et al., 2015, ApJS, 220, 12
Skelton R. E. et al., 2014, ApJS, 214, 24
Tanaka M., 2015, ApJ, 801, 20
Tanaka M. et al., 2018, PASJ, 70, S9
van der Wel A. et al., 2016, ApJS, 223, 29

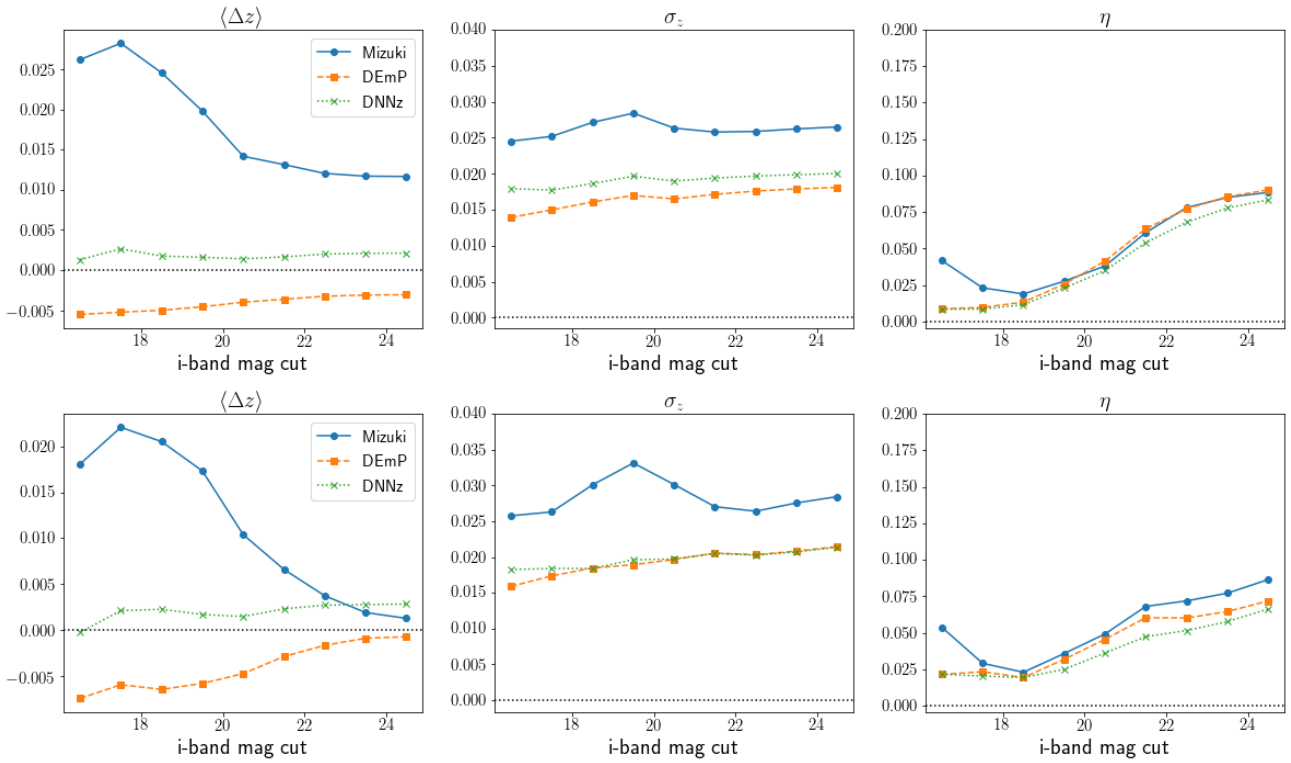

Fig. 2. photo-z statistics as a function of i-band magnitude cut, i.e. the horizontal axis denotes the faintest magnitude of the subsample. From left to right, mean bias, scatter and outlier rate. DEmP and DNNz shows well consistent accuracy while they are oppositely biased.

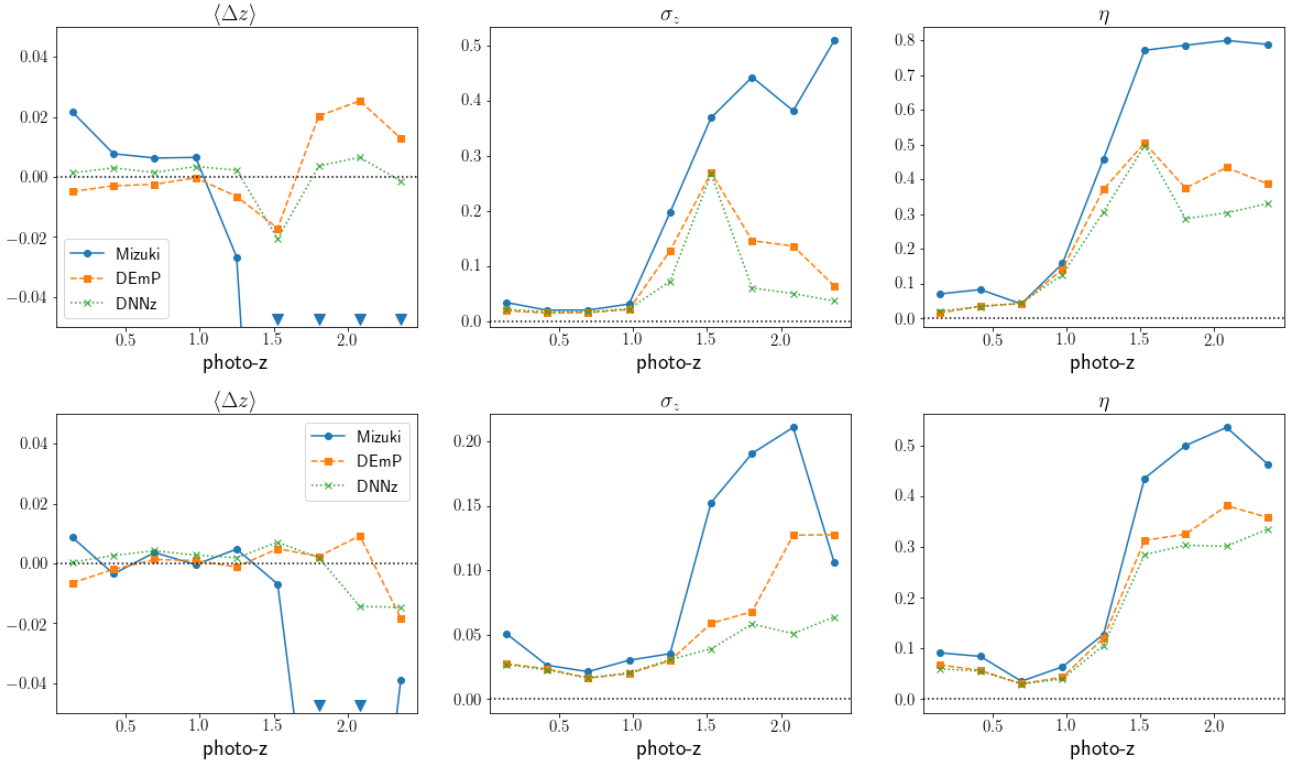

Fig. 3. Same as Fig. 2 but as a function of the photo-z.

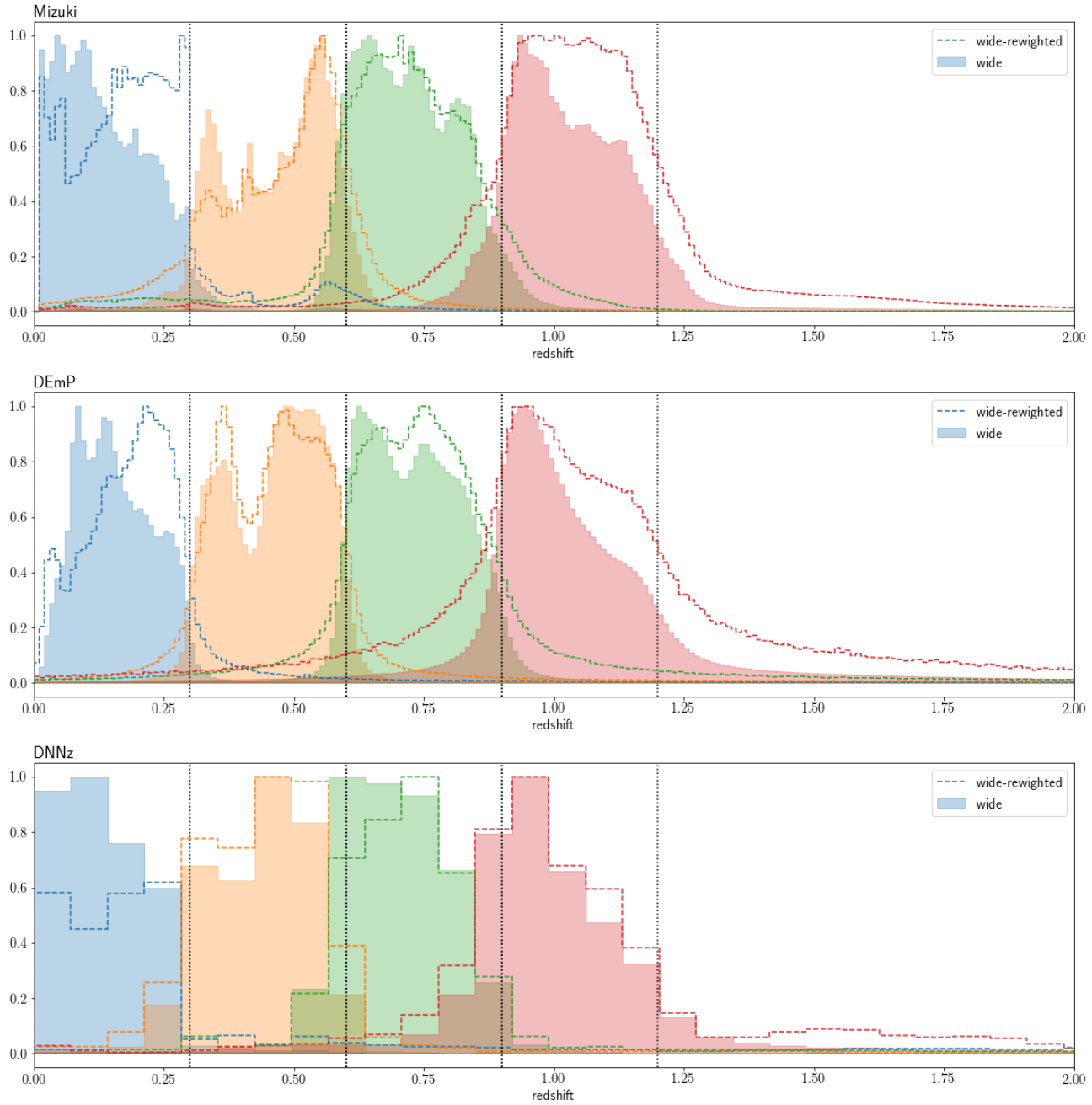

Fig. 4. dNdz distributions for binned samples. Shaded and dashed lines are for raw test sample and reweighted sample, respectively.

key	description
`object_id`	unique object id to be used to join with the photometry tables
`photoz_X`	Photo-z point estimate where X is either `mean`, `mode`, `median`, or `best`
`photoz_mc`	Monte Carlo draw from the full PDF
`photoz_conf_X`	Photo-z confidence value for `photoz_X`, defined by equation (15) of PDR1 paper
`photoz_risk_X`	Risk parameter for `photoz_X`, defined by equation (13) of PDR1 paper
`photoz_std_X`	Second order moment around a point estimate (`photoz_X`) derived from full PDF.
`photoz_err68_min`	16 % percentile in the PDF
`photoz_err68_max`	84 % percentile in the PDF
`photoz_err95_min`	2.5 % percentile in the PDF
`photoz_err95_max`	97.5 % percentile in the PDF

Table 1. Common photo-z quantities available for all the codes.

CODE	target selection	number of objects
`Mizuki`	`detect_is_primary` is `True`	214,484,923 (Wide)
	objects with CModel fluxes in at least three bands	18,383,344 (Deep/UltraDeep)
`DEmP`	`detect_is_primary` is `True`	507,215,723 (Wide)
		19,051,243 (Deep/UltraDeep)
`DNNz`	`detect_is_primary` is `True`	507,215,729 (Wide)
		19,051,243 (Deep/UltraDeep)

Table 2. Target selection and number of entries in the database.

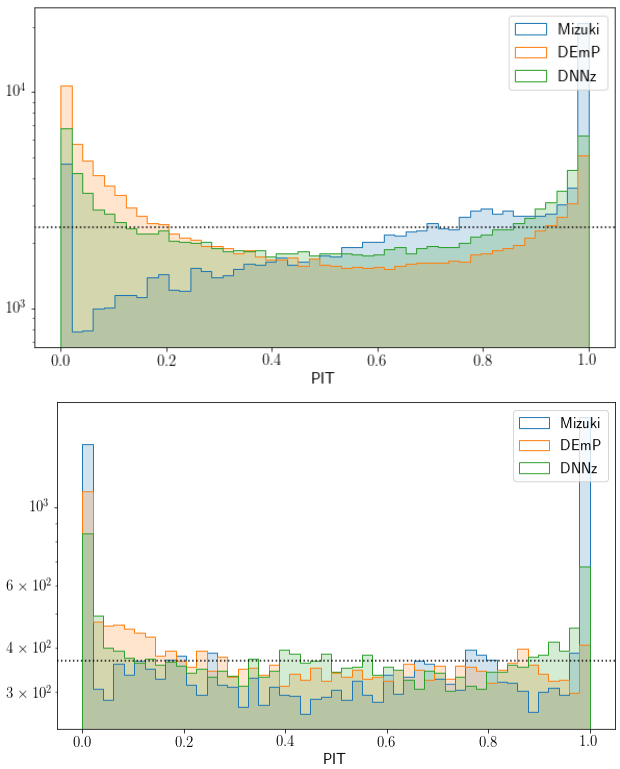

Fig. 5. The PIT distribution for wide (Top) and dud (Bottom). Horizontal dotted lines are just for guiding eyes.